Dalton Transactions

Nanoscale Li, Na, and K Ion-Conducting Polyphosphazenes by Atomic Layer Deposition

Journal:	*Dalton Transactions*
Manuscript ID	DT-ART-11-2021-003736.R1
Article Type:	Paper
Date Submitted by the Author:	22-Dec-2021
Complete List of Authors:	Nuwayhid, Ramsay; University of Maryland at College Park, Materials Science and Engineering Fontecha, Daniela; University of Maryland at College Park, Materials Science and Engineering Kozen, Alex; University of Maryland, Materials Science and Engineering Lee, Sang Bok; University of Maryland, Rubloff, Gary; University of Maryland, Materials Science and Engineering; University of Maryland Gregorzyck, Keith; University of Maryland, Department of Materials Science & Engineering

Nanoscale Li, Na, and K Ion-Conducting Polyphosphazenes by Atomic Layer Deposition

R. Blake Nuwayhid[1], Daniela Fontecha[1], Alexander C. Kozen[1], Sang Bok Lee[2], Gary W. Rubloff[2], and Keith E. Gregorczyk[1*]

[1]Department of Materials Science and Engineering, University of Maryland, College Park, MD 20742

[2]Department of Chemistry, University of Maryland, College Park, MD 20742

*Corresponding author: kgregorc@umd.edu

Abstract: A key trailblazer in the development of thin-film solid-state electrolytes has been lithium phosphorous oxynitride (LiPON), the success of which has led to recent progress in thin-film ion conductors. Here we compare the structural, electrochemical, and processing parameters between previously published LiPON and NaPON ALD processes with a novel ALD process for the K analogue potassium phosphorous oxynitride (KPON). In each ALD process, alkali *tert*-butoxides and diethylphosphoramidate are used as precursors. To understand the ALD surface reactions, this work proposes a reaction mechanism determined by *in-operando* mass spectrometry for the LiPON process as key to understanding the characteristics of the APON (A = Li, Na, K) family. As expected, NaPON and LiPON share similar reaction mechanisms as their structures are strikingly similar. KPON, however, exhibits similar ALD process parameters but the resulting film composition is quite different, showing little nitrogen incorporation and more closely resembling a phosphate glass. Due to the profound difference in structure, KPON likely undergoes an entirely different reaction mechanism. This paper presents a comprehensive summary of ALD ion conducting APON films as well as a perspective that highlights the versatility of ALD chemistries as a tool for the development of novel thin film ion-conductors.

1 Motivating Nanoscale Ion Conductors

As electronic devices and systems shrink, those with onboard battery power become increasingly limited by the size of the battery. This is particularly critical in applications where space is at a premium, such as implantable biomedical devices (i.e., cardiac pacemakers, cardiac defibrillators, neurostimulators, cochlear implants etc.), satellites, wearable electronics, and autonomous sensors.[1-3] Conventional battery architectures are difficult to shrink, in part because liquid electrolytes are retained in porous separators. The liquid electrolytes are flammable and produce toxic by-products when combusted or even exposed to air.[4-6] This increases safety concerns, particularly for implantable devices, where the consequences of failure are these same toxic chemicals leaking into the body cavity. Solid-state batteries (SSBs) are predicted to alleviate these safety concerns by replacing the liquid electrolyte with a solid material, referred to as solid-state electrolyte (SSE). To date however, the ionic conductivity of thin-film SSEs has not matched that of liquid electrolytes. Furthermore, replacing liquid electrolytes by their solid counterparts presents formidable obstacles – from forming high quality interfaces between electrodes and SSEs to altering battery manufacturing processes.

Our strategy is to design and fabricate nano- and micro-scale electrochemical energy storage devices using thin film fabrication as employed in semiconductor and related technologies to produce novel battery architectures.[7] In this way, we take advantage of decades of scalable manufacturing experience used for the fabrication of integrated chips (ICs), capacitors, solar panels, LCD screens, etc., where thin film fabrication is routinely employed to make very high density patterned 3D devices with extreme precision and success. High-aspect ratio structures have a similarly long history and have been used to increase the areal and volumetric densities of transistors, capacitors, and memory elements in CMOS fabricated devices. We use patterned nano-scale scaffold substrates such as etched silicon wafers and porous anodic aluminum oxide (AAO) to dramatically increase the active device surface area in the same two-dimensional footprint as non-patterned substrates.[8-10] This strategy necessitates the use of conformal deposition methods to fabricate our envisioned device architectures. Atomic layer deposition

(ALD) is an obvious choice as it is already used extensively in the semiconductor industry. ALD allows for the realization of this structure-based approach towards high-performance SSBs, of which we have demonstrated successful 3D energy storage devices such as an array of nanobatteries in nanoporous (AAO) and the first fully conformal 3D thin-film SSB.[8, 9]

2 Background

2.1 ALD Solid Electrolytes

Considering active battery components, SSE materials are most challenging, given that the materials and their solid phase are new to the battery industry. This has made process development for ALD SSEs a highly active and ongoing field of research, for which recent progress has been thoroughly summarized by Han *et al*.[11] The first attempts at ALD SSEs were based on well-established ALD processes (Al_2O_3, TaO_2, TiO_2, etc.) modified by the addition of Li, resulting in Li_2O-Al_2O_3 mixes[12], LiTaO[13], and LiAlSiO[14]. After these initial publications, two polymorphs of lithium phosphorous oxynitride (LiPON) were published nearly simultaneously. Our group published a quaternary plasma-enhanced ALD (PEALD) process using lithium *tert*-butoxide (LiO^tBu), H_2O, trimethyl phosphate (TMP), and plasma N_2, dosed sequentially without requiring super cycling.[15] The structural and electrochemical properties of LiPON are well known to be affected by N content[16, 17], and as such the resulting films demonstrated varying degrees of crystallinity and ionic conductivity. This ALD process demonstrated remarkable tunability of N up to 16 %. Simultaneously to our work, Nisula *et al.*[18] developed a simpler binary ALD process using Li hexamethyldisilazide (LiHMDS) and diethylphosphoramidate (DEPA). This process produced a material with an N/P ratio of 0.6 and overall stoichiometry of $LiPO_3N_{0.6}$. Impressed with the simplicity of Nisula's process and given our experience with LiO^tBu, we explored its reaction with DEPA. The results were different than both previously published ALD LiPON processes. The substitution of LiO^tBu for LiHMDS leads to full nitrogenation of LiPON, resulting in a N/P ratio of ~1 and an overall stoichiometry of Li_2PO_2N.[19] Further chemical analysis, discussed in detail in section 4, showed that the material contained chains of

primarily P-N=P bonds indicating a polyphosphazene like structure.[20] This unique LiPON process was a key enabler in the first fully conformal 3D thin-film SSB through its use as an ultrathin (40 nm) SSE.[8]

Several families of precursors have been tested for the purpose of introducing alkali cations into thin films by ALD. These include alkali trimethyl silanolates (TMSO), alkali hexamethyldisilazides (HMDS), alkali β-diketonates (thd), and alkali *tert*-butoxides (O^{t}Bu).[21-23] The most well studied family, however, are the *tert*-butoxides, with LiO^{t}Bu being the most common. It is part of a broader class of precursors called alkali *tert*-butoxides (AO^{t}Bu) which include Li, Na, K, Cs, and Rb substitutes. They are strong non-nucleophilic bases with the degree of basicity increasing with alkali metal ion size. In part, these compounds do not take place in nucleophilic addition reactions as a consequence of the steric hindrance of the central C atom.[24] They are best handled in an inert environment, as they react violently and exothermically with water, forming a lithium hydroxide shell and releasing *tert*-butyl alcohol vapor, which can self-ignite. Despite these reports, some ALD groups allow for brief air exposure when filling delivery containers and the precursors are found to be safe to handle in air briefly below 35˚C. In the vapor phase, AO^{t}Bu do not retain a monomeric structure and have been shown to oligomerize, with the size varying as a function of the alkali metal mass. The lithium and sodium versions are well known to form a hexamer structure, while the heavier potassium, rubidium, and cesium *tert*-butoxides form a tetramer with a cubanelike structure.[25-27] Sonsteby *et al.*[24] have written an extensive review on AO^{t}Bu's as precursors in ALD processes.

2.2 Polyphosphazenes

As mentioned, the reaction between LiO^{t}Bu and DEPA produces an inorganic polymer which can be classified as a polyphosphazene.[19] Polyphosphazenes are a well-studied class of inorganic polymers where the backbone structure contains no carbon, but rather repeating phosphorous and nitrogen atoms, with two substitute groups attached to each phosphorous atom as seen in Figure 1(a-c). They come in both cyclic and linear forms (Figure 1a and 1c). In most cases, the substitute groups are organic, leading

to poly(organo) phosphazenes. The earliest known compounds were produced by Liebig and Wohler when a small amount of hexachlorocyclotriphosphazene was produced in 1834. Intensive investigation began in the mid-1960s after techniques were developed to replace the halogen with organic substitutes.[20, 28] This led to a wide variety of organophosphazenes being synthesized and studied.

The materials discussed in this paper can be classified as poly(alkali) phosphazenes where the substitute groups attached to the phosphorous atoms are O^--A^+ (where A is Li, Na, or K). A depiction of an ideal alkali polyphosphazene chain is displayed in Figure 1b, along with 3D molecular structures of the linear and cyclic alkali polyphosphazene. While our focus is on ion conducting thin films, *tert*-butoxides present the broader ALD community an opportunity to study not only other alkali *tert*-butoxides to elucidate the reaction chemistry (the focus of this work) but, potentially a much broader class of materials where the substitution at the phosphorous atom is a functional organic group.

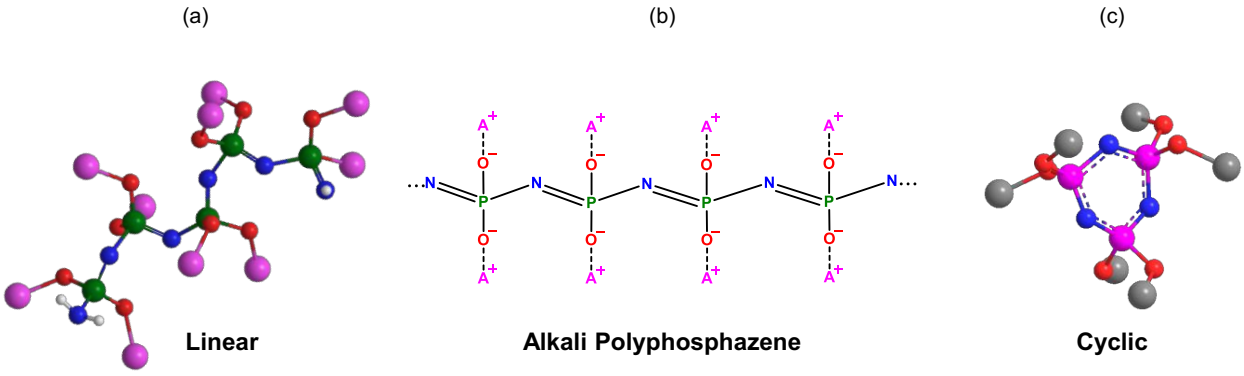

Figure 1. Molecular structure of an ideal alkali polyphosphazene. (a) 3D linear representation, (b) 2D structure based on the Li_2PO_2N structure described in this work[19], (c) 3D cyclic representation. The alkali ion $A^+ = Li^+, Na^+, K^+$.

2.3 Lithium Phosphorous Oxynitride

Though the body of work for ALD ion conductors continues to grow, the most well-studied material is LiPON due to it attractive voltage stability window, its self-passivating interfaces, and large body of prior development work on the material using PVD.[29] LiPON was first developed as a sputtered SSE at Oak Ridge National Laboratory in the early 1990's by Bates *et al.*[30, 31] Even with this long history, the phosphorous oxynitride (PON) structure has been challenging to understand due its amorphous nature. Despite this difficulty, there are several aspects of the bonding environment that are indicative of the structure and resulting properties. LiPON is part of a broader family of APON materials where the properties, including structure and ionic conductivity, are directly linked to the amount and coordination state of nitrogen in the film.[16, 17]

X-ray photoelectron spectroscopy (XPS) is the most common technique to characterize LiPON, in which the binding environment of the amorphous PON network can be determined. Bates *et al.*[30, 31] initially assigned two nitrogen states based on the XPS spectra of LiPON, a doubly coordinated nitrogen state (N_d, P-N=P) at low binding energy and a triply coordinated nitrogen state (N_t, P-N<P) at higher binding energy. This agreed with earlier work in the 1980s on bulk nitrided lithium and sodium metaphosphate ($Li/NaPO_3$) glasses.[32, 33] This convention continued and is most common for thin-film LiPON. However, it should be mentioned that Dudney and colleagues[34] recently suggested LiPON possesses only singly coordinated, or apical nitrogen (N_a, P-N) and N_d based on simulations and neutron scattering experiments to resolve the amorphous structure. Their simulations on LiPON with varying degree of N content imply the structure contained only N_a and N_d, and was in strong agreement with neutron scattering pair distribution function analysis on sputtered LiPON. It is important to note that the LiPON studied by Dudney and colleagues[34] was produced by sputtering, resulting in a stoichiometry of $Li_{2.94}PO_{3.50}N_{0.31}$. Furthermore, the authors mentioned they could not completely rule out the presence of N_t in the sputtered LiPON examined. This LiPON composition differs from that of our ALD LiPON

(Li_2PO_2N)[19], implying that the connectivity of the PON backbone may vary in polymorphs of LiPON. Due to the recent discrepancies and for consistency, we stick with the assignment of N_d and N_t for the APONs reported in this work.

2.4 Goal

This work compares the reaction parameters, resulting chemical structure, and ion conducting properties of our two previously published LiPON and NaPON processes with new data that looks at the reaction between KO^tBu and DEPA. Section 3 discusses the ALD process parameters through *in-operando* spectroscopic ellipsometry (SE). The chemical structure of the three materials is discussed in section 4, where *in-vacuo* transfer to an XPS allowed for the measurement of pristine materials without contamination from air exposure. While the Li and Na substituted versions are shown to have very similar structures, interestingly the K version incorporates little N (2.2% max.), despite showing the presence of P. Next, in section 5, we present *in-operando* mass spectrometry data for the (LiO^tBu + DEPA) LiPON process where we attempt to elucidate the reaction chemistry that leads to the unique polyphosphazene structure. In light of the structure and reaction chemistry of ALD LiPON, we propose a surface reaction scheme in section 6. In section 7, we discuss the electrochemical properties of the resulting thin films. Finally, we discuss, in a more holistic fashion, the implications of these materials from both an ALD process and application standpoint.

3 ALD Process Parameters

As discussed, LiO^tBu has been widely used as a precursor in ALD processes due to the pressing interest in applying ALD in Li battery technology.[35, 36] The use of NaO^tBu and KO^tBu in ALD processes is growing with the recent interest in beyond Li-ion chemistries as well as applications in piezo/ferro-electric materials.[24] AO^tBu's inherently possess low vapor pressure, requiring higher temperature heating than

most commonly used ALD precursors, and thus require bubbler assisted delivery to the ALD reactor. For the purposes of this discussion, we will focus on the AO^{t}Bu + DEPA ALD process chemistries.

To understand the vaporization behavior of the AO^{t}Bu's, thermogravimetric analysis (TGA) was conducted and compared to the literature. Figure 2 shows the TGA curves measured for Li-, Na-, and KO^{t}Bu, in which all precursors display similar sublimation behavior. First, there is a small initial mass loss around 50 °C, corresponding to the release of crystal *tert*-butanol.[24] The onset temperature of vaporization is ~150 °C and proceeds in a single step for all precursors. These findings are well within literature values where available.[22, 27] The residual mass varies from ~5% for LiO^{t}Bu to ~12% for the K and Na substitutes. This additional residual mass is most likely due to the brief air exposure that forms alkali oxide and hydroxide decomposition products. The onset temperature for AO^{t}Bu decomposition is determined at the intersection of the starting mass baseline with the tangent to the point of maximum inflection of the curve.[37] The onset temperature for degradation was found to be 220 °C for LiO^{t}Bu, 240 °C for KO^{t}Bu, and 250°C for NaO^{t}Bu. The thermal stability of the *tert*-butoxides does not follow the usual trend related to increasing size of the alkali ion, and is instead due to the vapor-phase oligomeric structure. KO^{t}Bu crystalizes as a tetrameric cubane-like structure, making the overall complex smaller and lighter than the NaO^{t}Bu hexameric structure.[24-27]

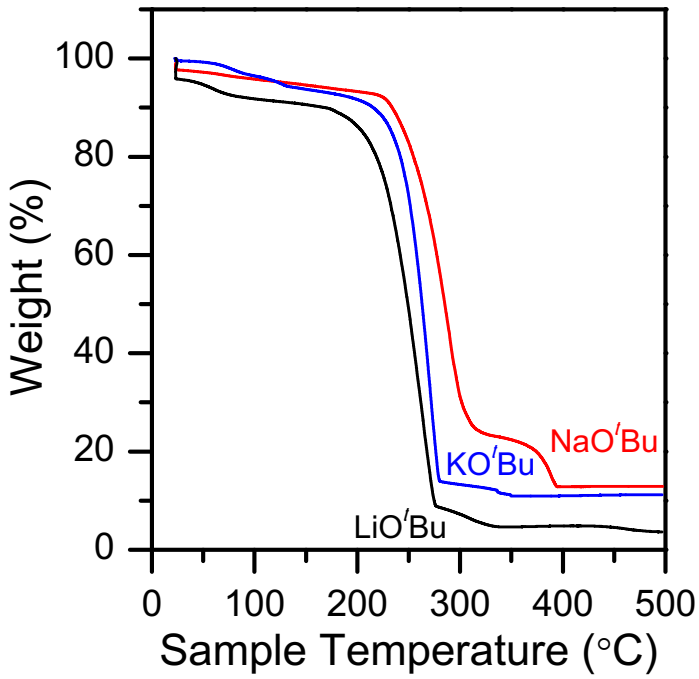

Figure 2. Thermogravimetric analysis of alkali *tert*-butoxides. AOtBu's were heated at a rate of 5 °C/ min under N_2 flow.

ALD process parameters were evaluated using *in-operando* SE, with the process results shown in Figure 3a-c. Figure 3a shows the growth per cycle (GPC) of the AO^{t}Bu-DEPA processes as a function of temperature with a 20 s AO^{t}Bu and 2 s DEPA pulse. All processes display features of a thermally activated process but are not ideal ALD reactions. The GPC of LiPON was measured to be ~0.9 Å/cycle at 300 °C, whereas the GPC of NaPON and KPON were only ~0.1 and ~0.2 Å/cycle, respectively, at this same temperature. Temperatures of 375 °C were required for GPCs near 1 Å/cycle for NaPON and KPON. The NaPON and KPON processes have nearly identical temperature windows, both shifted ~50-100 °C higher than that of LiPON at comparable growth rates. Though, the GPC of KPON is slightly higher than NaPON at 275-325 °C, which is explained through the lower thermal stability of the KO^{t}Bu precursor than NaO^{t}Bu in Figure 2. The GPC as a function of AO^{t}Bu dosage with a constant DEPA pulse of 2s is shown in Figure 3b. In the LiO^{t}Bu case, the GPC increases from ~0.5 Å/cycle with a 5 s pulse and nearly saturates at ~0.9 Å/cycle

above a 20s pulse. Similar trends are seen for NaO^{t}Bu and KO^{t}Bu. NaO^{t}Bu shows a similar GPC of ~0.5 Å/cycle with a 5 s pulse, increasing to ~0.7 Å/cycle at 30s. The LiO^{t}Bu pulse study took place at 300 °C, while the Na- and KO^{t}Bu pulse studies were deposited at 375 °C. All three processes show linear, step-wise growth as a function of time or cycle number, as seen in Figure 3c.

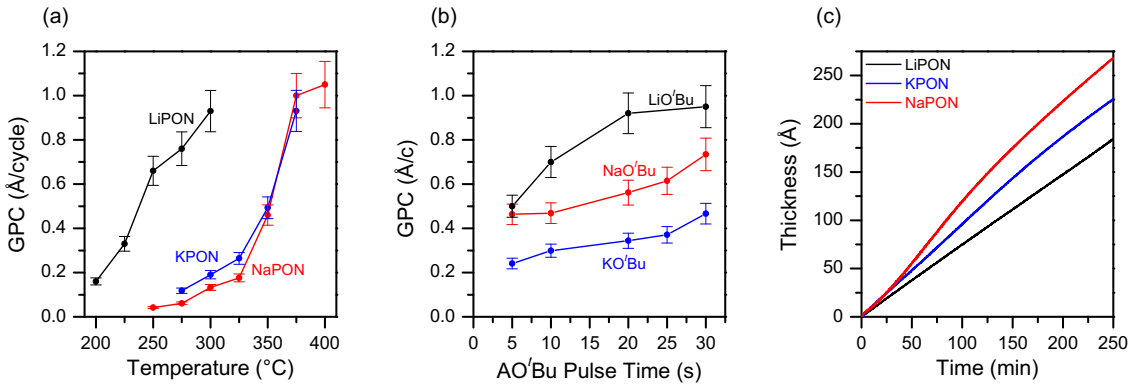

Figure 3. ALD process parameters of LiPON, NaPON, and KPON measured by *in-operando* spectroscopic ellipsometry. (a) Growth per cycle as a function of reactor temperature. (b) Growth per cycle as a function of AO^{t}Bu pulse time. The LiO^{t}Bu pulse study was deposited at 300 °C, while the NaO^{t}Bu and KO^{t}Bu pulse study were deposited at 350 °C. The DEPA pulse was fixed at 2 s. (c) Thickness profile for LiPON (deposited 250°C), NaPON (deposited 375°C), and KPON (deposited 375°C).

The three AO^{t}Bu-DEPA processes for A = Li, Na, K explored here exhibit similar ALD growth characteristics, requiring relatively high temperatures for desirable growth rates (i.e., 1 Å/cycle). The higher temperatures required for comparable growth of NaPON/KPON as compared to LiPON are attributed to the larger atomic radius of the alkali ion and bulkier complexes formed in the gas phase.[24-27] Though the ALD processes exhibit linear growth at fixed precursor doses, the lack of a clear temperature window suggests some CVD-like precursor decomposition contributing to enhanced growth rates. This behavior is more obvious in the case of NaPON and KPON, as the higher growth temperatures are above that of their respective AO^{t}Bu's decomposition window as evidenced by the TGA (Figure 2). LiO^{t}Bu displays the most desirable ALD characteristics of the AO^{t}Bu's examined here, growing at lower temperatures, and

exhibiting self-limiting reactions of each precursor pulse. Na- and KO^{t}Bu have been demonstrated to be self-limiting with H_2O in growing Na and K aluminates[27], so perhaps introducing a H_2O pulse between the AO^{t}Bu and DEPA pulse would be worth investigating. Nonetheless, the thermal reactions of Li-, Na-, and KO^{t}Bu with DEPA are desirable for highly chemically consistent ALD processes with fine tunability and extreme conformality.

4 Chemical Structure

We determine the structure of the alkali polyphosphazenes through XPS using *in-vacuo* transfer from the ALD chamber directly to the XPS chamber. Figure 4 shows the compositional information derived from XPS measurements for LiPON (Figure 4a), NaPON (Figure 4b), and KPON (Figure 4c) as a function of deposition temperature. LiPON exhibits a stable P/N ratio of 1 throughout the deposition temperature window, and the lowest total carbon content among the alkali polyphosphazenes, which decreases with increasing deposition temperature from 16.8% to 10% at the expense of Li and O. NaPON, shown in Figure 4b, has a remarkably stable chemistry throughout its temperature window from 300 ˚C to 375 ˚C, with a P/N ratio also near 1. However, unlike LiPON, NaPON shows significantly increased alkali metal content (~35% Na vs ~25% Li), which occurs at the expense of decreased P and N content. Carbon contamination in NaPON is also higher than LiPON, with carbon levels at ~18% for all deposition temperatures. Figure 4c shows the chemistry of KPON from 275˚C to 375˚C. While there is phosphorous present in these films increasing with the temperature, there is negligible nitrogen incorporated, with a maximum of 2.2% nitrogen incorporated at 375˚C, and the P/N ratio is far from one. With significantly more oxygen and carbon and less nitrogen than either LiPON or NaPON, this indicates scission of the amine ligand in the DEPA molecule during the deposition process, further indicating deviations from the ideal reaction mechanism. The resulting stoichiometry of the films are Li_2PO_2NC, $Na_4PO_3NC_2$, and $K_{5.2}PO_{6.3}N_{0.16}C_{4.7}$ respectively.

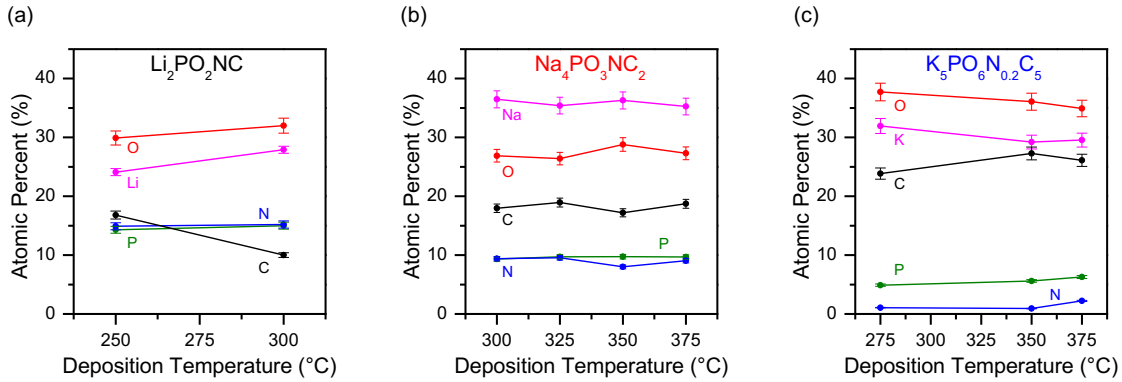

Figure 4. Elemental composition of (a) LiPON, (b) NaPON, and (c) KPON as a function of deposition temperature as determined by XPS without air-exposure of the films.

Figure 5 shows the high-resolution XPS regions for the constituent elements in LiPON, NaPON, and KPON. The alkali metal spectra (Figure 5a,f,k) all exhibit a single alkali-oxygen bonding state. The high-resolution spectra for LiPON displays a single peak in the P 2p region (Figure 5b), representing the backbone of the polyphosphazene chain. Two peaks are observed in the O 1s spectra (Figure 5c), with a major peak at 530.3 eV representing non-bridging oxygen ($P\text{-}O^{-}Li^{+}$) and a minor peak at 531.3 eV representing a bridging oxygen species (P-O-P or P-O-C). The N 1s region (Figure 5d) exhibits two peaks consistent with doubly coordinated nitrogen (N_d, P-N=P) and triply coordinated nitrogen (N_t, P-N<P_2) bonding environments at 397.0 eV and 398.4 eV. N_t substitutes for N_d in the polyphosphazene chain, causing some deviation from the ideal -PO_2N_2- backbone. The C 1s region (Figure 5e) shows the presence of primarily hydrocarbon species (284.8 eV), with some –C-O- bonding (286.1 and 289.3 eV). This minor contribution is due to the incorporation of residual *tert*-butoxide/ethoxy ligands from the precursors. The ideal polyphosphazene would possess all N_d nitrogen and no carbon, but excluding carbon the resulting stoichiometry of Li_2PO_2N represents a lithium polyphosphazene.

The high-resolution XPS regions for NaPON (Figure 5f-j) indicate a strikingly similar material to LiPON. However, the NaPON exhibits increased P-N<P_2 content, resulting in a N_d/N_t ratio of 2.2 compared to 3.7 for LiPON. This indicates additional disorder in the ideal -PO_2N_2- backbone chains, and increased C-O bonding present in the films. The resolution of a distinct C-O peak is indistinguishable in the O 1s core-level spectra (Figure 5h), despite the O 1s region displaying a single sharp peak with a full-width-half-maximum (FWHM) of 1.24. This peak can therefore be attributed to contributions from Na^+-$^-$O and C-O. It is possible that the close proximity of the Na KLL peak at 536.4 eV makes clear assignment of a distinct C-O peak difficult.

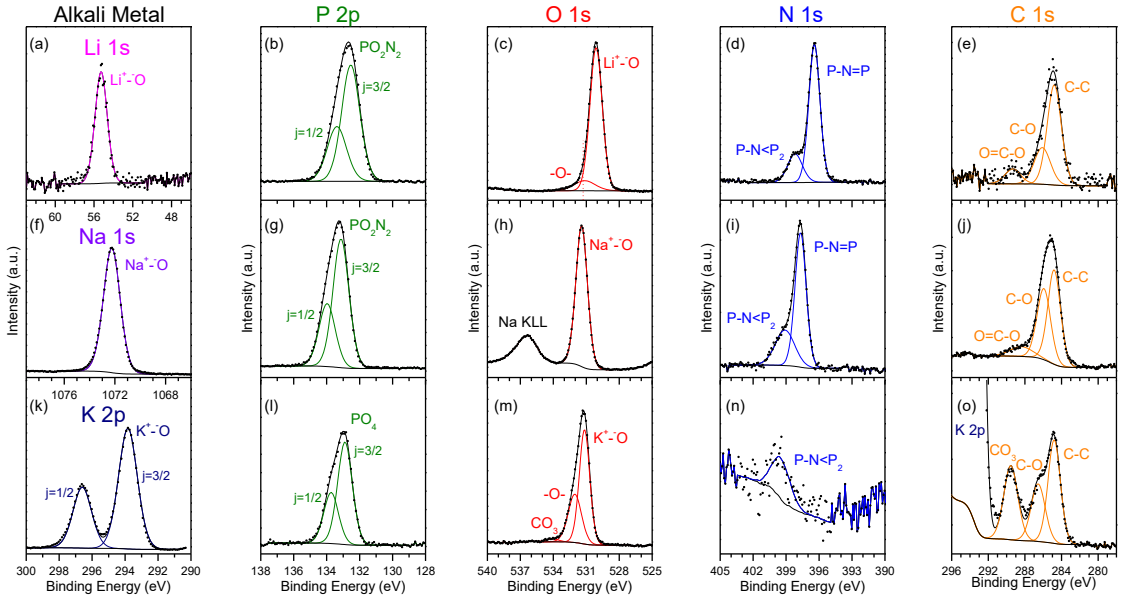

Figure 5. High-resolution core-level XPS spectra for the elements of interest of (a-e) LiPON deposited at 300 °C, (f-j) NaPON deposited at 350 °C, and (k-o) KPON deposited at 350 °C. All spectra are calibrated to the C-C peak at 284.8 eV.

Most interesting are the high resolution XPS figures for KPON, shown in Figure 5k-o, revealing a dramatically different material from both LiPON and NaPON. The P 2p region (Figure 5l) indicates a bonding environment consistent with PO_4 tetrahedra, indicating negligible P-N chain bonding. The O 1s spectra in Figure 5m indicates the presence of non-bridging oxygen at 531.2 eV (P-O$^-$-K^+) and bridging

oxygen at 532.0 eV (P-O-P, or P-O-C) typically observed in a phosphate. However, there is an additional peak indicative of carbonate formation due to the peak at 534.1 eV. The N 1s region, (Figure 5n) indicates negligible nitrogen (0.92%) in the films, with a single peak at 399.5 eV associated with N_t, representing disorder of the PO_4 unit and an absence of P-N=P backbone chains. The C 1s spectra (Figure 5o) shows the presence of C-C and C-O bonds as in LiPON and NaPON, but also shows an additional peak at 289.6 eV, consistent with carbonate formation in the material.

As discussed previously, the ALD LiPON and NaPON films can both be classified as polyphosphazenes (N/P=1).[19, 38] Remarkably, while the NaPON process produces a film nearly structurally identical to the thermal LiPON ALD process, the resulting stoichiometry (Na_4PO_3N vs. Li_2PO_2N) does not indicate a simple replacement of Na with Li. Furthermore, when KO^tBu is reacted with DEPA in the same manner, similar growth characteristics are observed as in NaPON, but negligible nitrogen is incorporated into the film.

5 Understanding the Surface Reaction

In-operando quadrupole mass spectrometry (QMS) was employed to elucidate the surface reactions that enable the growth mechanisms of the Li/NaPON ALD processes, which can provide insight into and further unravel the film composition (XPS) and growth kinetics (SE) of the ALD APONs. As a case study, we first examined the LiPON ALD process to carefully characterize surface reactions before moving to the more complicated NaO^tBu/KO^tBu-DEPA processes. The mass spectra of the individual precursors in the ALD reactor are first examined, along with the surface decomposition of LiO^tBu, and then time-resolved QMS is used to infer the surface reaction mechanism.

5.1 Mass spectra of LiO^tBu

The mass spectrum of LiO^tBu was determined by QMS sampling of individual precursor pulses to understand their fragmentation/cracking pattern and thus distinguish from background species. Figure 6a

shows the mass spectrum of LiO^{t}Bu compared with that of the background Ar flow in the ALD reactor. Distinguishable peaks are observed over the Ar background at *m/z* = 15 (CH_3^+), 31 (CH_3O^+), 42 ($C_3H_6^+$/$C_2H_2O^+$), and 59 ($C_3H_7O^+$). These masses represent the cracking pattern of *tert*-butanol (*t*-BuOH), as supported by the close agreement with the mass spectrum for *t*-BuOH in the NIST reference database.[39] The fragmentation of *t*-BuOH in the mass spectrometer proceeds by the pathways described in Figure 6b, resulting in the ion fragments at *m/z* 15, 31, 43, and 59. The peak at *m/z* = 42 is most likely $C_3H_6^+$, which appears from deprotonation of the C_3H_7 (*m/z* = 43) fragment. Due to their higher intensities, *m/z* = 31 (CH_3O^+) and 59 ($C_3H_7O^+$) will be used to track LiO^{t}Bu during the ALD process.

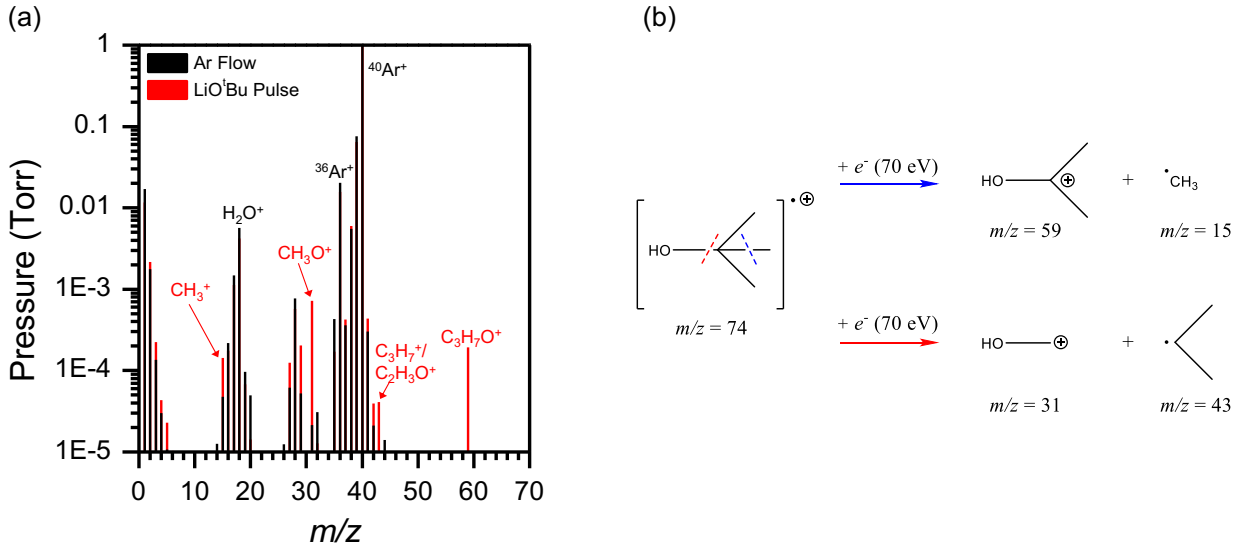

Figure 6. (a) Fragmentation pattern of LiO^{t}Bu measured by *in-operando* mass spectrometry in the ALD reactor. The fragmentation pattern was obtained during precursor dose in the reactor with Ar flow and is overlayed with the background spectra of the reactor under Ar flow. (b) proposed fragmentation patterns of *t*-BuOH in the QMS.

The mass spectrum for LiO^{t}Bu did not display direct fragmentations of LiO^{t}Bu, but instead those representing *t*-BuOH. This was expected, as Hornsveld et al.[40] also observed this in their QMS study of a Li_2CO_3 ALD process using LiO^{t}Bu as the lithium source. The mass spectrum of pure LiO^{t}Bu is not available in the NIST Standard Reference Database[39], however direct vapor phase measurements of LiO^{t}Bu have been reported using time of flight mass spectrometry.[41, 42] These results showed a fragmentation pattern

of peaks corresponding to $Li_nR_{n-1}^+$ species (R = *t*-BuO), evidencing that Li*O*^{t}Bu forms a hexamer in the gas phase. However, such high masses are outside the detectable range of our ALD coupled QMS (1-300 amu) used in this study, and the high reactor pressure and small precursor dose lessens sensitivity. For instance, the base peak of the Li*O*^{t}Bu hexamer, $[Li_6(t\text{-BuO})_5]^+$ has a *m/z* of 407. Therefore, while direct observation of Li*O*^{t}Bu is not possible, its presence is monitored through *tert*-butanol.

5.2 Surface Decomposition of LiO^{t}Bu

To complement QMS measurements, XPS analysis was performed on a Si wafer subjected to Li*O*^{t}Bu pulses at 250 °C. High-resolution scans of the Li 1s and O1s are shown in Figure 7. Deconvolution of the XPS spectra shows 2 peaks of equal atomic ratios corresponding to a 3:1 ratio of Li_2O:LiOH. The overall film composition was $Li_{1.6}O$ with negligible carbon content (~0.6%), suggesting that Li*O*^{t}Bu is depositing as mixed Li_2O/LiOH on the Si surface. This finding is not in line with the proposed chemisorption of Li*O*^{t}Bu during its initial pulse in Li_2CO_3 and LiOH ALD processes by Cavanagh et al.[43] Chemisorption suggests that Li*O*^{t}Bu remains intact on the surface and does not initially release volatile reaction byproducts such as *t*-BuOH until a subsequent H_2O dose occurs. Hornsveld et al.[40] reported QMS data supporting such chemisorption behavior, in which the signal of *t*-BuOH (*m/z* 59) is negligible during Li*O*^{t}Bu dose compared to a spike observed during the subsequent H_2O pulse. In our work, a significant increase in *m/z* 59 is observed with repeated Li*O*^{t}Bu pulses (Figure S2). This discrepancy can be attributed to the lower reactor temperature of 150 °C used by Hornsveld and colleagues, compared to 250 °C in this work. Based off our measurements, we can conclude that Li*O*^{t}Bu readily decomposes to Li_2O and LiOH at our ALD temperatures. This behavior is expected based on the TGA of Li*O*^{t}Bu shown in Figure 2. This also supports the non-self-limiting nature observed for the A*O*^{t}Bu's in Figure 3, as the GPC continues to increase with longer A*O*^{t}Bu pulses due to prolonged thermal decomposition on the surface.

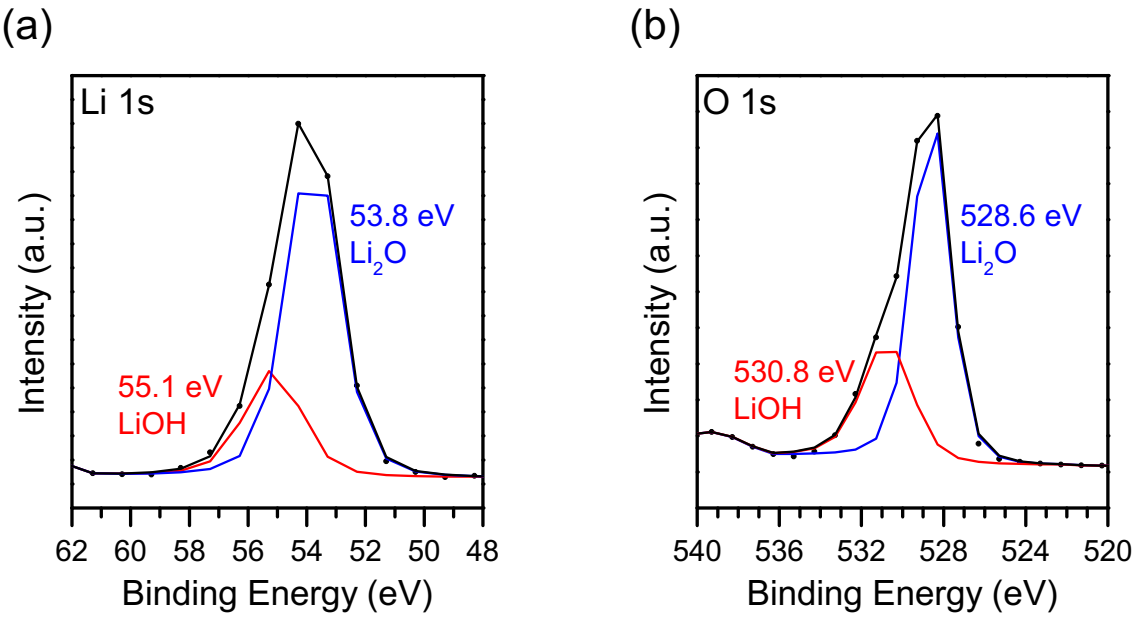

Figure 7. XPS Spectra of LiO^tBu pulsed on a Si wafer at 240 °C. (a) Li 1s and (b) O 1s high-resolution core-level spectra.

5.3 Mass Spectra of DEPA

In Figure 8a, the mass spectrum of DEPA shows distinguishable peaks at *m/z* = 16 (O^+), 17 (OH^+/NH_2^+), 27 ($C_2H_3^+$), 29 ($C_2H_5^+/CHO^+$), and 45 ($C_2H_5O^+$). These peaks are in agreement with the mass spectrum of DEPA in the NIST Standard Reference Database[39], differing slightly in intensity distribution. The mass spectrum of DEPA in the NIST database shows the base peak at *m/z* = 80, then, in descending order, at *m/z* = 98, 126, 81, 108, 109, 29, 27, 45, 124. However, we were unable to distinguish masses above 70 from the background noise with the scan settings during a DEPA pulse into the ALD reactor. We did however observe all of these masses when DEPA was sampled into the QMS directly from a heated cylinder, bypassing the ALD reactor (Figure S3). In Figure S3, peaks at *m/z* = 16, 17, 18, 27, 28, and 29 are still the most intense, likely indicating a boost in signal from background H_2O and N_2 in the lines. The molecular fragmentation pathway of DEPA is described in Figure 8b. Variations in ion fragmentations arise from the electron bombardment process, e.g. $[M\text{-}CH_3CH_2]^{\bullet+}$ = 124 vs. $[M\text{-}CHCH_2]^{\bullet+}$ = 126. The peaks at *m/z*

= 28 and 45 will be used to track DEPA during the ALD process due to higher intensity and distinguishability from LiO^{t}Bu fragments and background species.

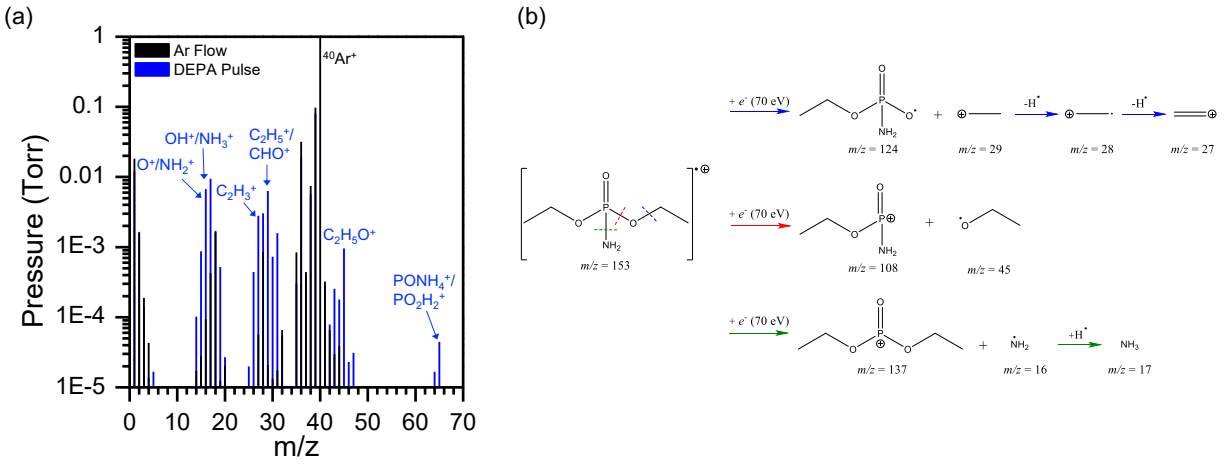

Figure 8. (a) Fragmentation pattern of DEPA measured by *in-operando* mass spectrometry in the ALD reactor. The fragmentation pattern was obtained during precursor dose in the reactor with Ar flow and is overlayed with the background spectra of the reactor under Ar flow. (b) Proposed fragmentation patterns of DEPA in the QMS.

5.4 Time-resolved Mass Spectra of LiPON Process.

With the fragmentation patterns of both precursors well understood, a modified ALD recipe was developed for *in-operando* monitoring of the LiPON process via QMS. The recipe included modified pulse/purge times to assist in distinguishing between reactants/products. The modified recipe is described in Table 1 below.

Table 1. Modified ALD recipe for *in-operando* QMS sampling.

	Precursor	Pulse Time (s)	Purge Time (s)	Cycles
Step 1a	*LiO^{t}Bu*	15	5	1
Step 1b	*LiO^{t}Bu*	5	5	6
Step 1c	*LiO^{t}Bu*	2	4	3
Step 2	*DEPA*	8	5	2
Step 3a	*LiO^{t}Bu*	15	5	2
Step 3b	*LiO^{t}Bu*	2	4	3
Step 4a	*DEPA*	2	4	1
Step 4b	*DEPA*	2	6	4

In step 1, a long LiO^{t}Bu pulse is introduced to create a stable reference measurement, followed by shorter repetitive pulses to ensure saturation of the reactive surface and dose stabilization through the needle valve to the QMS. In step 2, two long DEPA pulses are introduced to fully react with the surface and generate a high concentration of byproducts. In step 3, multiple LiO^{t}Bu pulses are introduced to again ensure that the dose is large enough to fully saturate the surface. In Step 4, DEPA is pulsed with shorter purge times to observe the reaction byproduct, followed by 4 pulses with slightly longer purge times to determine if the surface is saturated with DEPA molecules. This modified ALD recipe is helpful in distinguishing between reactants/products detected in the QMS. Steps 1-4 represent 1 complete cycle of the modified ALD process. Two full cycles are shown in Figure 9.

Figure 9 shows the time resolved QMS data for this modified ALD process. Based on the experiments discussed in sections 5.1 and 5.3, *m/z* 28 ($C_2H_4^+$) and 45 ($C_2H_5O^+$) were chosen to track DEPA, *m/z* 59 ($C_3H_7O^+$) was used to track LiO^{t}Bu, and *m/z* 40 (Ar^+) was used for reference. In step 1, ion fragment 59 tracks with the Ar peak at *m/z* 40, as Ar is used to aid in the delivery of low vapor pressure LiO^{t}Bu to the reactor. Following The LiO^{t}Bu dose in step 1, *m/z* 59 signal decreases to ~2 x 10^{-5} Torr until the leading DEPA pulse in step 2. In the first DEPA pulse of step 2, *m/z* 28 and 59 see an immediate sharp increase, whereas *m/z* 45 increases with a delayed response. The second DEPA pulse shows a small uptick in the decreasing signals of *m/z* 28 and 59, and an additional peak at *m/z* 45. In step 3, DEPA contributions

continue to decrease, with increases in *m/z* 59 at each LiO^{t}Bu pulse. In step 4, the first DEPA pulse shows a large increase in *m/z* 28 and 45, with an additional sharp increase in *m/z* 59. The subsequent DEPA pulses show little or no contribution of *m/z* 59 and saturation of DEPA in the reactor. Step 2 is the most insightful mechanistically to the ALD process and clearly shows when DEPA is pulsed, *t*-BuOH (*m/z* = 59) is immediately released, followed by the release of ethanol (EtOH, *m/z* 45).

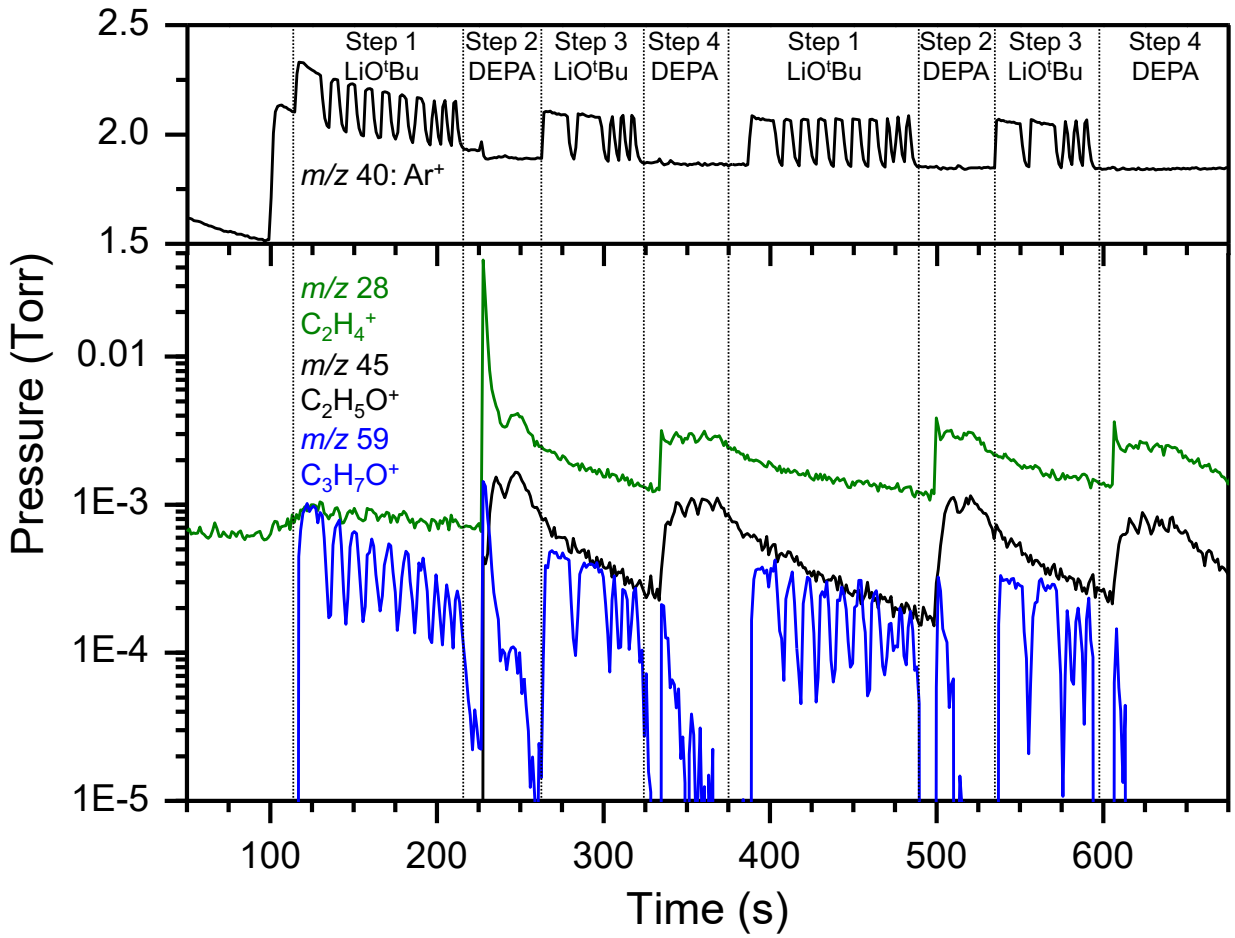

Figure 9. Time-resolved mass spectra for 2 complete cycles of the modified LiPON ALD process at 250 °C. Fragments are shown for *m/z* = 40 (Ar$^+$), 28 ($C_2H_4^+$, DEPA), 45 ($C_2H_5O^+$, DEPA), and 59 ($C_3H_7O^+$, LiO^{t}Bu).

6 Proposed Reaction Mechanism

Given the chemical composition of the materials (Section 4) and the detailed QMS studies (Section 5), we propose the following mechanism for the LiPON ALD process, shown in Figure 10. Upon initial pulse of LiO^tBu, OH surface species are replaced with O-Li, forming a surface lithium alkoxide and releasing t-BuOH. The remaining OH groups on the surface represent the incomplete replacement of the O-H bond with O-Li. Li_2O is shown to represent some thermal decomposition of LiO^tBu. For the following reaction steps shown, we assume all LiO^tBu reacted in the first step or was otherwise purged out of the reactor. In the subsequent DEPA pulse, the DEPA molecule remains mostly intact, binding to the Li-O surface and releasing *t*-BuOH (*m/z* 59) forming a Li-O-($PO_2NH_2CH_2CH_3$) bond through the release of ethane (*m/z* 28) from DEPA. A surface mediated polymerization then occurs where neighboring P-N bonds link, releasing ethanol (*m/z* 45) as a byproduct. In the following LiO^tBu pulse, N from the surface interacts with LiO^tBu, causing the tert-butoxide to scavenge the H atom in the amine group, leaving as *t*-BuOH (*m/z* 59). The P=N bond is then formed by a resonance rearrangement from the P=O bond to form P-O-Li and movement of electron density from Li-N to N-O. This reaction sequence results in the polyphosphazene chain-like structure Li_2PO_2N. We note this is an idealized reaction mechanism to form the pure Li_2PO_2N polyphosphazene. The true ALD reaction will involve some thermal decomposition of precursors and side reactions resulting in incomplete surface binding/release of precursor ligands and the excess carbon content observed in the film. These initial experiments provide evidence for a plausible reaction mechanism.

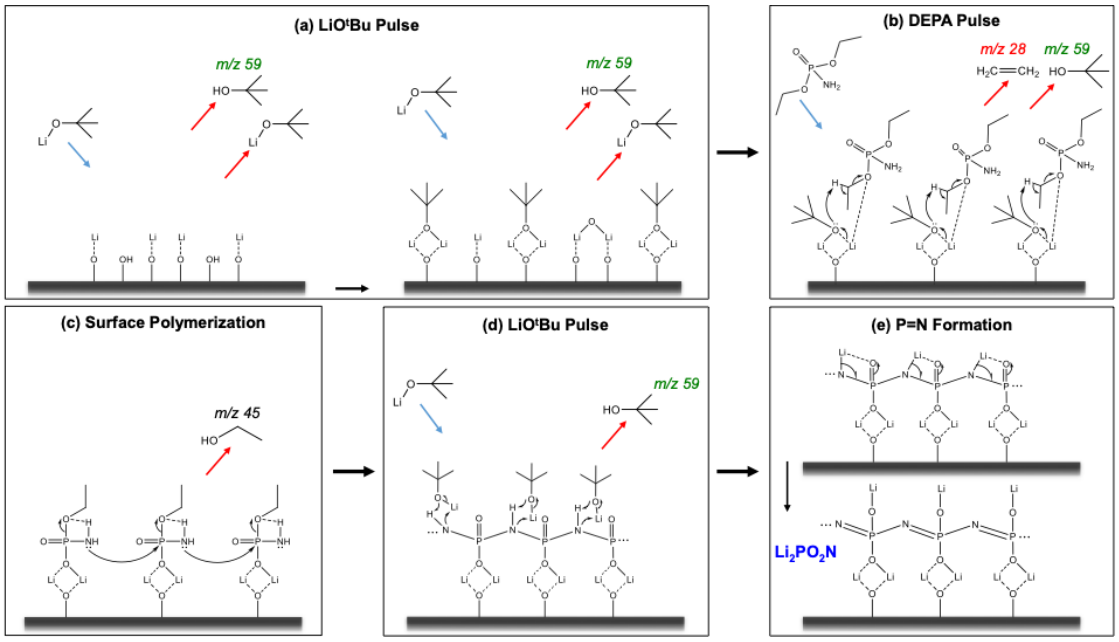

Figure 10. Proposed Thermal LiPON Reaction Mechanism. The reaction mechanism is based on *in-situ* mass spectrometry measurements of the ALD process. (a) LiO^{t}Bu chemisorbs on hydroxylated surface. (b) DEPA reacts with the lithium alkoxide surface to release C_2H_4 and $C(CH_3)_3OH$. (c) Linking of the surface species occurs through the P-N bonds with the loss of CH_3CH_2O. (d) LiO^{t}Bu interacts with the N atoms in the chain and leads to the resonance rearrangement to form P=N. (e) The alternating P=N bond in the chain forms the basis for the polyphosphazene Li_2PO_2N structure.

7 Electrochemistry

The alkali PONs discussed herein are functional ionic materials, meaning they allow ion transport while offering negligible electronic conductivity. The most important metrics for SSE applications are the ionic conductivity and activation energy. Devices for testing were fabricated by depositing the ALD APON between metal electrodes in a metal-electrolyte-metal (MEM) stack. The ionic transport properties of LiPON, NaPON, and KPON were measured through electrochemical impedance spectroscopy (EIS). Activation energy for ion transport in LiPON and NaPON is determined from temperature-based measurements. Electrochemical analysis is presented for all APONs that were exposed to air and also for pristine MEM devices fabricated and tested in a custom UHV-Ar glovebox cluster system (Figure S4).

EIS measurements for all three materials are shown as Nyquist plots in Figure 11. Test devices were prepared by depositing the APON between Pt blocking electrodes, requiring brief air exposure for deposition of the top Pt contact. The EIS spectra of LiPON and NaPON show similar behavior with a semicircular arc at high-mid frequencies and an increase in the imaginary impedance component at low frequencies. The semicircular arc is attributed to ion transport through the electrolyte and is assigned two parallel-resistor constant phase element (CPE) components in the equivalent circuit used to model the curves (Figure 9a inset). The two CPEs represent bulk ionic conduction of the APON film (CPE_b), and ion conduction through an air-reacted interphase layer (CPE_r) formed at the surface. The sharp increase in the low frequency regime is modeled by a CPE in series (CPE_W) with the CPE_b and CPE_r to account for Warburg diffusion in the blocking electrode. We use this equivalent circuit model to calculate the total resistance ($R_b + R_r$) of the film, from which we determine its ionic conductivity. LiPON exhibited an ionic conductivity of 1.6×10^{-7} S/cm at 35 °C, 2 orders of magnitude higher than that of NaPON at 25 °C (1.3×10^{-9} S/cm). The EIS spectra of the K substituted version differs in that it shows only two semicircles with no Warburg-like diffusion. As in the prior cases, this curve is modeled by two CPE components, CPE_b and CPE_r, but does not include a Warburg element. Interestingly, the ionic conductivity of KPON was measured to be 7.4×10^{-9} S/cm at 25 °C. This his higher than that of NaPON at room temperature, despite the larger ionic radius of K^+ than Na^+. The shape of the EIS curve of KPON suggests that the material acts as an electrostatic capacitor. It is unclear why KPON does not display any semi-infinite diffusion and surprisingly displays a lower overall resistance than NaPON. The different ionic behavior of KPON than LiPON and NaPON supports its deviation in structure from the Li and Na analogues. EIS testing at lower frequencies may be required to gain a better understanding of the ionic transport properties of KPON, as the measurements in Figure 11 were recorded with a cutoff frequency of 500 mHz.

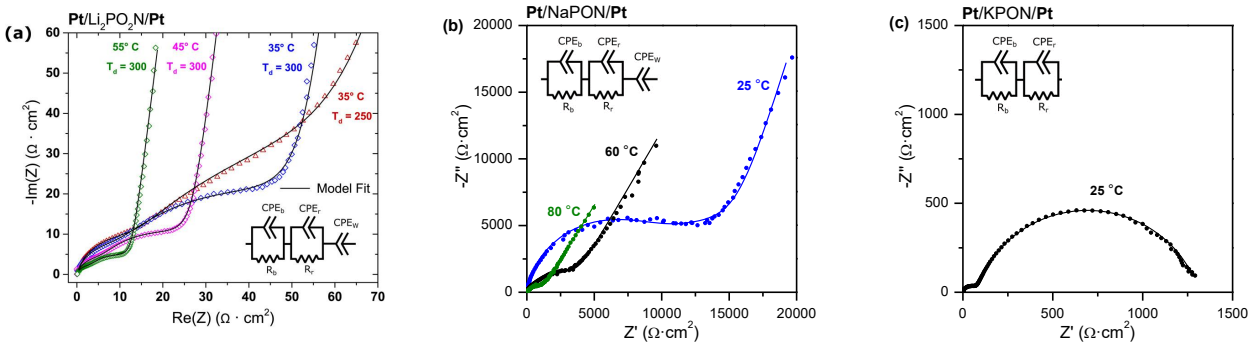

Figure 11. EIS measurements of APONs. (a) Nyquist plots for Pt/80 nm LiPON/Pt devices measured between 35 -55 °C. LiPON was deposited at 300°C and 250 °C (red curve). Adapted from ref 19. Copyright 2017 American Chemical Society. (b) Nyquist plots for Pt/137 nm NaPON/Pt devices measured between 25-80 °C. NaPON was deposited at 375 °C. Adapted from ref 38. Copyright 2020 American Chemical Society. (c) Nyquist plot for Pt/97 nm KPON/Pt devices measured at 25 °C. KPON was deposited at 375 °C. All samples were briefly exposed to air for deposition of the top Pt metal blocking electrodes.

To consider the true ionic properties of the APON SSE films without the effects of an impeding interphase layer, measurements of LiPON and NaPON were also conducted while eliminating air exposure. Figure 12a-b shows temperature based EIS measurements of pristine LiPON and NaPON. Measurements on Pt/LiPON/Li reveal an increased conductivity of 3.7×10^{-7} S/cm at room temperature. A similar trend is observed for pristine NaPON, exhibiting an increase in ionic conductivity to 1.0×10^{-7} S/cm at room temperature, and up to 2.5×10^{-6} S/cm at 80 °C. The Arrhenius plot in Figure 12c for LiPON and Figure 12d for NaPON show that the activation energies for air-exposed and pristine samples are nearly identical for both LiPON and NaPON. The activation energy for air-exposed LiPON and NaPON is 0.64 eV and 0.66 eV, respectively. The activation energy of pristine LiPON and NaPON is 0.55 eV and 0.53 eV, respectively. The lower activation energy associated with pristine samples clearly indicates the removal of an resistive interphase layer as the energy barrier for ion migration is lowered. The similar activation energies additionally identify that the energy barrier for Li^+/Na^+ migration relies primarily on the amorphous phosphorus oxynitride network, i.e. the energy barrier for ionic movement is independent of the ionic species but not the overall chemical structure.

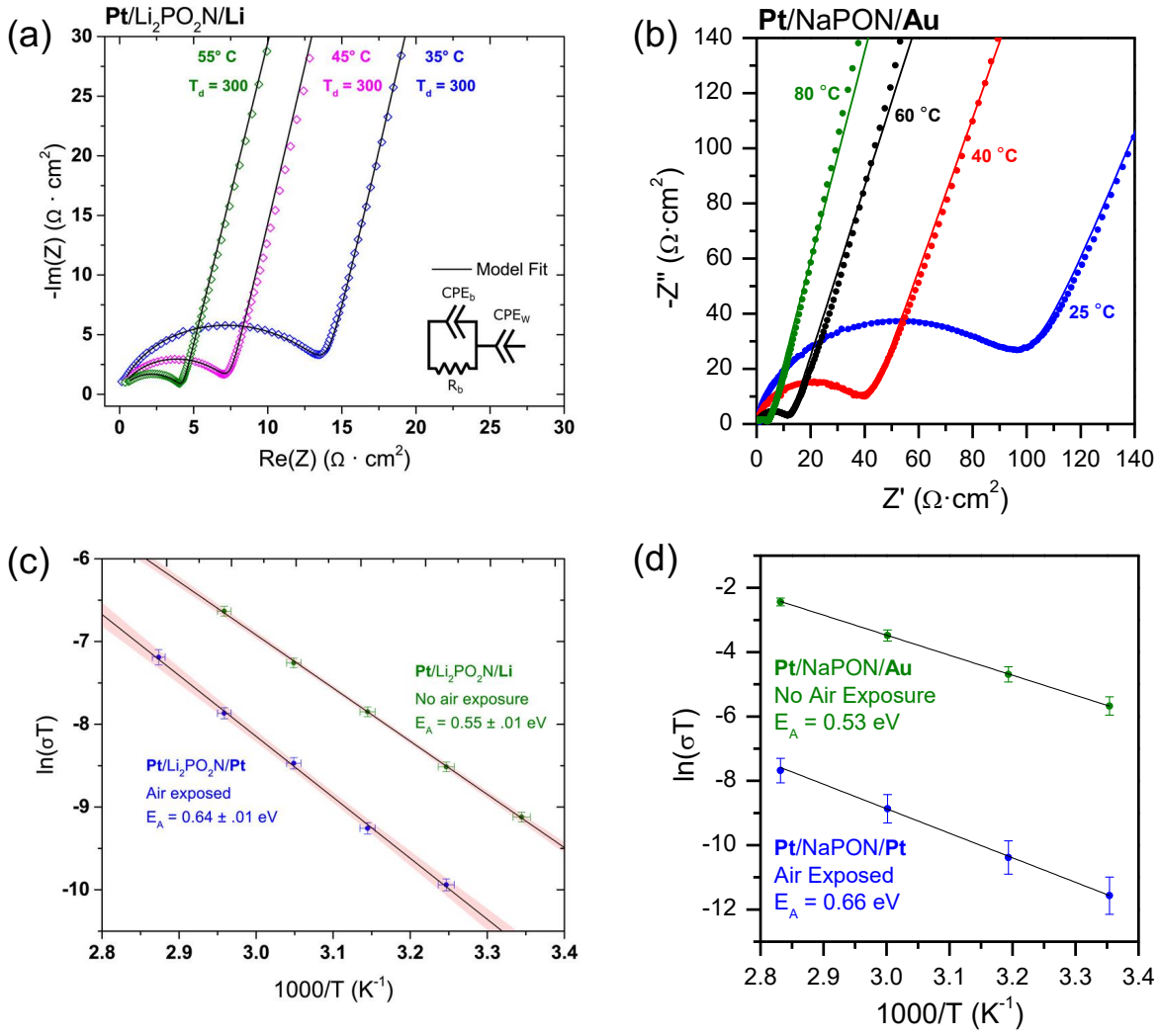

Figure 12. Transport properties of LiPON and NaPON without air exposure. (a) Nyquist plots for Li/80 nm LiPON/Pt measured between 35-55 °C. (b) Nyquist plot for Au/137 nm NaPON/Pt measured between 25-80 °C. (c) Arrhenius plots for air-exposed and pristine LiPON films showing activation energies of the films. (d) Arrhenius plots for air-exposed and pristine NaPON films showing activation energies of the films. (a) and (c) adapted from ref 19. Copyright 2017 American Chemical Society. (b) and (d) adapted from ref 38. Copyright 2020 American Chemical Society.

8 Discussion

Through additional *in-operando* QMS studies we hope to explain differences in the LiPON/NaPON/KPON ALD processes to better understand the surface-mediated reactions of AO^{t}Bu's and DEPA. Initial QMS data of NaO^{t}Bu pulsed into the ALD reactor indicates that NaO^{t}Bu is detectable in the QMS as *t*-BuOH, just as the case for LiO^{t}Bu (Figure S5). The similar cracking pattern in the QMS and phosphazene structure indicated by XPS (P:N=1) allow us to speculate that ALD NaPON proceeds in a similar reaction mechanism to LiPON, though a more thorough study would be required to confirm this assumption. The resulting films possess differences in stoichiometry, Li_2PO_2NC vs. $Na_4PO_3NC_2$. This is not surprising given the higher deposition temperatures of NaPON required for comparable growth to LiPON, i.e. 375 °C vs. 300 °C. The higher process temperature provides opportunity for increased thermal decomposition of the NaO^{t}Bu precursor, thus producing more incorporated *tert*-butoxy and ethoxy ligands in the film.

The KPON process presents a completely different reaction mechanism, as little nitrogen (2.2% max.) is incorporated into the film. The composition of the film is instead found to be a ratio of K_3PO_4/K_2CO_3/KO^{t}Bu. The different reactivity towards DEPA is attributed to the KO^{t}Bu precursor. KO^{t}Bu is bulkier and a stronger base than its Li and Na counterparts. The increased steric hindrance is believed to play a role in the different reactivity of KO^{t}Bu towards DEPA. *In-operando* QMS of KO^{t}Bu-DEPA would aid in understanding the reaction mechanism by distinguishing different species desorbing from the surface than the LiPON and NaPON processes. Furthermore, in an attempt to develop an ALD process for a fully nitrogenated KPON film, alternative reaction schemes should be performed. For instance, we have had success growing LiPON and NaPON plasma-based ALD processes[15], which are essentially Li_3PO_4/Na_3PO_4 processes with an added nitrogen plasma pulse to dope the alkali phosphate. The base potassium

phosphate has not been demonstrated but is believed to be plausible, based on the simple reaction sequence of AO^{t}Bu-H_2O-TMP. In addition, the large presence of phosphate in the potassium film deposited herein is promising. The addition of N_2 plasma to a K_3PO_4 process may be able to overcome the steric energy barrier to incorporate nitrogen into the film. If this proves unsuccessful, further novel precursors are worth exploring.

Alkali PONs are advantageous SSE materials due to their amorphous glassy structure. Crystalline SSEs have been developed by ALD but require high temperature annealing thus limiting material and application compatibility, in addition to introducing significant thermal stress. Of amorphous ALD SSEs, only Li_xSiO[44] and Li_3BO_3-Li_2CO_3 (LBCO)[45] possess a higher room temperature ionic conductivity than ALD LiPON, exhibiting ionic conductivities of 1.5 and 2.2 × 10^{-6} S/cm, respectively. Looking forward, thin-film SSEs with higher ionic conductivities are certainly desirable. Building upon the LBCO process, replacing the Li_2CO_3 component with Li_3N or Li_3PO_4 may improve the ionic conductivity as lithium phosphate and nitride have a higher ionic conductivity than lithium carbonate. Additionally, substituting Li_xSiO with N to make a Li_xSiON glassy material may improve the ionic conductivity in a similar manner to LiPON, in which the substituting nitrogen for oxygen is known to decrease electrostatic interactions with Li in LiPON films and improve the Li^+ transport. For beyond LIBs, NaPON is a promising SSE for Na ion batteries. The ionic conductivity reported above for NaPON is on par with that of LiPON. Similar to the other glassy materials for Li ion batteries, the Na-based analogues are worth exploring due to the similar chemistries. In the processes of Li_xSiO and LBCO, LiO^{t}Bu is used as the Li source, so substitution with NaO^{t}Bu is worth implementing to synthesize the Na analogues. Although it should be mentioned, as evidenced in this work, the processes are not an exact one-for-one exchange of NaO^{t}Bu for LiO^{t}Bu, or more clearly represented in the case of KO^{t}Bu.

While we have worked on a few of the alkali polyphosphazenes through ALD, there remains a vast expanse of materials unexplored. Interesting possibilities building upon this work include organic linked

phosphazene chains, mixed alkali ion conductors, and divalent alkaline earth phosphazenes. By replacing the alkali cations with any of the enumerable organic ligand groups, a wide range of materials with an equally wide range of potential properties remain undiscovered. Additionally, this work calls for additional ALD work on mixed alkali metal conductors. This could be possible through super cycles of processes for the alkali oxides/oxynitrides/nitrides/phosphates. Sonsteby et al.[46, 47] have demonstrated a mixed $KNbO_3$-$NaNbO_3$ using KO^tBu and NaO^tBu as precursors. It was found that the K:Na ratio was tunable to 1% by substituting in NaO^tBu for KO^tBu in the $KNbO_3$ process. Following a similar approach may be possible for the mixing of LiPON/NaPON processes described herein.

The development of divalent ionic conductors looks to be more challenging. A MgP_xO_y ALD SSE has been reported, but exhibited non-ideal electrochemical performance with a temperature of 500 °C required to obtain an ionic conductivity of 1.6×10^{-7} S/cm and high activation energy of 1.37 eV.[48] In terms of Ca ALD, a Ca phosphate glass resembling a hydroxyapatite ($Ca_{10}(PO_4)_6$) structure has been demonstrated, but no ionic properties were reported.[23] Unlike the alkali metal precursors, di-*tert*-butoxides are not ideal ALD precursors. Ca and Mg based cyclopentadienyl (Cp) and β-diketonates (thd) precursors have proven to be the most desirable for alkaline earth metal deposition.[49] Beyond batteries and ferro/piezo-electronic devices, the APONs presented here are of interest for applications in next generation neuromorphic computing. Realization of neuromorphic computing requires interfacing with neurons, which may require the use of Na^+ and K^+ conductors. The fabrication of functional sensors that are integrable with biological systems are therefore of high interest.

9 Summary and Conclusions

Table 2. Summary of ALD Deposition, Chemical Composition, and Ionic Properties of APONs.

	LiPON	**NaPON**	**KPON**
ALD Temperature Window (°C)	200-300	300-375	300-375
Growth Per Cycle (Å/cycle)	0.16-0.93	0.13-1.0	0.19-0.93
Stoichiometry	Li_2PO_2NC	$Na_4PO_3NC_2$	$K_5PO_6N_{0.2}C_5$
Ionic Conductivity at 25 °C (S/cm)	3.7×10^{-7}	1.0×10^{-7}	7.4×10^{-9}
Activation Energy (eV)	0.55	0.53	-

In this paper we have presented a new ALD process of potassium phosporous oxynitride and compared it to our previous work on ALD LiPON and NaPON. Their ALD process conditions, chemical composition, and ionic properties are summarized in Table 2. The LiPON ALD process was found to exhibit the most desirable properties. Deposition of LiPON with adequate growth rates was demonstrated at relatively low temperatures, in addition to obtaining the lowest carbon contamination (~10%), and the highest overall ionic conductivity (3.7×10^{-7} S/cm at 25 °C).

NaPON required temperatures ~100 °C higher than that of LiPON for comparable growth rates. The structure of NaPON is in strong agreement with LiPON, confirming its classification as a polyphosphazene, with additional disruption of the P-N=P backbone and carbon incorporation. NaPON's ionic conductivity was on the same order of magnitude of LiPON (10^{-7} S/cm) and exhibited nearly the same activation energy. This supports the XPS results indicating that the structural configuration of NaPON and LiPON are similar, as the modes of ionic conduction through the polyphosphazene chain are energetically similar despite the increased size of Na^+ compared to Li^+.

The ALD process parameters for KPON revealed very similar growth kinetics over the temperature range of 300-375 °C to that of NaPON. Despite the similarity in ALD process parameters, the chemistry of the K-based film was quite different. KO^tBu-DEPA reacted to produce a film with little N content and its XPS analysis more closely resembled a K_3PO_4/K_2CO_3 film. The difference in reactivity of the film is

attributed to increased steric bulk of the KO^tBu precursor, and increased degree of basicity compared to Li- and NaO^tBu. The similarities in growth rates to the NaPON process are indicative of the thermal decomposition facilitated growth of these processes due to their similarities in sublimation behavior determined by TGA. The ionic properties of KPON are promising, as it exhibited an ionic conductivity of 7.4×10^{-9} S/cm at room temperature with brief air exposure, which is slightly higher than that of air-exposed NaPON. KPON would be expected to follow a similar trend as that of LiPON/NaPON and exhibit a further increase in ionic conductivity for a pristine film. As mentioned, further electrochemical characterization of KPON is necessary to fully understand its ionic transport behavior and provide a direct comparison to NaPON and LiPON.

Author Contributions

R.B.N., K.E.G., and G.W.R. developed the research plan. R.B.N. performed the experiments described in this paper with guidance from A.C.K. and K.E.G. S.B.L. provided insight to the mass spectrometry analysis and reaction mechanism. R.B.N., K.E.G., and D.F wrote the manuscript. All authors discussed and approved the final version of the manuscript.

Acknowledgements

This work was supported as part of the Nanostructures for Electrical Energy Storage (NEES), an Energy Frontier Research Center (EFRC) funded by the U.S. Department of Energy, Office of Science, Office of Basic Energy Sciences, under Award no. DESC0001160. We acknowledge the support of the Maryland Nanocenter, including its FabLab for use of deposition tools. Daniela Fontecha was supported by the National Science Foundation Graduate Research Fellowship Program under Grant No. DGE 1840340. Any opinions, findings, and conclusions or recommendations expressed in this material are those of the author(s) and do not necessarily reflect the views of the National Science Foundation.

Conflicts of Interest

The authors declare no conflicts of interest.

References

1. J. F. M. Oudenhoven, L. Baggetto and P. H. L. Notten, *Advanced Energy Materials*, 2011, **1**, 10-33.
2. F. L. Cras, B. Pecquenard, V. Dubois, V.-P. Phan and D. Guy-Bouyssou, *Advanced Energy Materials*, 2015, **5**, 1501061.
3. Y. Khan, A. E. Ostfeld, C. M. Lochner, A. Pierre and A. C. Arias, *Advanced Materials*, 2016, **28**, 4373-4395.
4. K. Takada, *Acta Materialia*, 2013, **61**, 759-770.
5. C. Sun, J. Liu, Y. Gong, D. P. Wilkinson and J. Zhang, *Nano Energy*, 2017, **33**, 363-386.
6. A. Manthiram, X. Yu and S. Wang, *Nature Reviews Materials*, 2017, **2**, 16103.
7. M. Noked, C. Liu, J. Hu, K. Gregorczyk, G. W. Rubloff and S. B. Lee, *Accounts of Chemical Research*, 2016, **49**, 2336-2346.
8. A. Pearse, T. Schmitt, E. Sahadeo, D. M. Stewart, A. Kozen, K. Gerasopoulos, A. A. Talin, S. B. Lee, G. W. Rubloff and K. E. Gregorczyk, *ACS Nano*, 2018, **12**, 4286-4294.
9. C. Liu, E. I. Gillette, X. Chen, A. J. Pearse, A. C. Kozen, M. A. Schroeder, K. E. Gregorczyk, S. B. Lee and G. W. Rubloff, *Nature Nanotechnology*, 2014, **9**, 1031-1039.
10. P. Banerjee, I. Perez, L. Henn-Lecordier, S. B. Lee and G. W. Rubloff, *Nature Nanotechnology*, 2009, **4**, 292-296.
11. L. Han, C.-T. Hsieh, B. Chandra Mallick, J. Li and Y. Ashraf Gandomi, *Nanoscale Advances*, 2021, **3**, 2728-2740.
12. T. Aaltonen, O. Nilsen, A. Magrasó and H. Fjellvåg, *Chemistry of Materials*, 2011, **23**, 4669-4675.
13. J. Liu, M. N. Banis, X. Li, A. Lushington, M. Cai, R. Li, T.-K. Sham and X. Sun, *The Journal of Physical Chemistry C*, 2013, **117**, 20260-20267.
14. Y.-C. Perng, J. Cho, S. Y. Sun, D. Membreno, N. Cirigliano, B. Dunn and J. P. Chang, *J. Mater. Chem. A*, 2014, **2**, 9566-9573.
15. A. C. Kozen, A. J. Pearse, C.-F. Lin, M. Noked and G. W. Rubloff, *Chemistry of Materials*, 2015, **27**, 5324-5331.
16. B. Fleutot, B. Pecquenard, H. Martinez, M. Letellier and A. Levasseur, *Solid State Ionics*, 2011, **186**, 29-36.
17. B. Wang, B. S. Kwak, B. C. Sales and J. B. Bates, *Journal of Non-Crystalline Solids*, 1995, **183**, 297-306.
18. M. Nisula, Y. Shindo, H. Koga and M. Karppinen, *Chemistry of Materials*, 2015, **27**, 6987-6993.
19. A. J. Pearse, T. E. Schmitt, E. J. Fuller, F. El-Gabaly, C.-F. Lin, K. Gerasopoulos, A. C. Kozen, A. A. Talin, G. Rubloff and K. E. Gregorczyk, *Chemistry of Materials*, 2017, **29**, 3740-3753.
20. H. R. Allcock, *Chemical Reviews*, 1972, **72**, 315-356.
21. A. Ruud, V. Miikkulainen, K. Mizohata, H. Fjellvåg and O. Nilsen, *Journal of Vacuum Science & Technology A*, 2017, **35**, 01B133.
22. J. Hämäläinen, J. Holopainen, F. Munnik, T. Hatanpää, M. Heikkilä, M. Ritala and M. Leskelä, *Journal of The Electrochemical Society*, 2012, **159**, A259-A263.
23. M. Putkonen, T. Sajavaara, P. Rahkila, L. Xu, S. Cheng, L. Niinistö and H. J. Whitlow, *Thin Solid Films*, 2009, **517**, 5819-5824.

24. H. H. Sønsteby, J. E. Bratvold, V. A. L. K. Killi, D. Choudhury, J. W. Elam, H. Fjellvåg and O. Nilsen, *Journal of Vacuum Science & Technology A*, 2020, **38**.
25. M. H. Chisholm, S. R. Drake, A. A. Naiini and W. E. Streib, *Polyhedron*, 1991, **10**, 337-345.
26. H. Nekola, F. Olbrich and U. Behrens, *Zeitschrift für anorganische und allgemeine Chemie*, 2002, **628**, 2067-2070.
27. E. Ostreng, H. H. Sonsteby, S. Oien, O. Nilsen and H. Fjellvag, *Dalton Trans*, 2014, **43**, 16666-16672.
28. H. R. Allcock, J. L. Desorcie and G. H. Riding, *Polyhedron*, 1987, **6**, 119-157.
29. J. D. LaCoste, A. Zakutayev and L. Fei, *The Journal of Physical Chemistry C*, 2021, **125**, 3651-3667.
30. J. B. Bates, N. J. Dudney, G. R. Gruzalski, R. A. Zuhr, A. Choudhury, C. F. Luck and J. D. Robertson, *Journal of Power Sources*, 1993, **43**, 103-110.
31. J. B. Bates, N. J. Dudney, G. R. Gruzalski, R. A. Zuhr, A. Choudhury, C. F. Luck and J. D. Robertson, *Solid State Ionics*, 1992, **53-56**, 647-654.
32. R. Marchand, D. Agliz, L. Boukbir and A. Quemerais, *Journal of Non-Crystalline Solids*, 1988, **103**, 35-44.
33. R. K. Brow, M. R. Reidmeyer and D. E. Day, *Journal of Non-Crystalline Solids*, 1988, **99**, 178-189.
34. V. Lacivita, A. S. Westover, A. Kercher, N. D. Phillip, G. Yang, G. Veith, G. Ceder and N. J. Dudney, *J Am Chem Soc*, 2018, **140**, 11029-11038.
35. L. Ma, R. B. Nuwayhid, T. Wu, Y. Lei, K. Amine and J. Lu, *Advanced Materials Interfaces*, 2016, **3**, 1600564.
36. S. Moitzheim, B. Put and P. M. Vereecken, *Advanced Materials Interfaces*, 2019, **6**.
37. A. W. Coats and J. P. Redfern, *Analyst*, 1963, **88**, 906-924.
38. R. B. Nuwayhid, A. Jarry, G. W. Rubloff and K. E. Gregorczyk, *ACS Applied Materials & Interfaces*, 2020, **12**, 21641-21650.
39. *Journal*.
40. N. Hornsveld, W. M. M. Kessels and M. Creatore, *The Journal of Physical Chemistry C*, 2019, **123**, 4109-4115.
41. J. D. Kahn, A. Haag and P. v. R. Schleyer, *The Journal of Physical Chemistry*, 1988, **92**, 212-220.
42. G. E. Hartwell and T. L. Brown, *Inorganic Chemistry*, 1966, **5**, 1257-1259.
43. A. S. Cavanagh, Y. Lee, B. Yoon and S. George, *ECS transactions*, 2010, **33**, 223.
44. B. Wang, J. Liu, M. Norouzi Banis, Q. Sun, Y. Zhao, R. Li, T.-K. Sham and X. Sun, *ACS Applied Materials & Interfaces*, 2017, **9**, 31786-31793.
45. E. Kazyak, K.-H. Chen, A. L. Davis, S. Yu, A. J. Sanchez, J. Lasso, A. R. Bielinski, T. Thompson, J. Sakamoto, D. J. Siegel and N. P. Dasgupta, *J. Mater. Chem. A*, 2018, **6**, 19425-19437.
46. H. H. Sonsteby, O. Nilsen and H. Fjellvag, *Glob Chall*, 2019, **3**, 1800114.
47. H. H. Sønsteby, O. Nilsen and H. Fjellvåg, *Journal of Vacuum Science & Technology A: Vacuum, Surfaces, and Films*, 2016, **34**.
48. J. Su, T. Tsuruoka, T. Tsujita, Y. Nishitani, K. Nakura and K. Terabe, *Chemistry of Materials*, 2019, **31**, 5566-5575.
49. V. Miikkulainen, M. Leskelä, M. Ritala and R. L. Puurunen, *Journal of Applied Physics*, 2013, **113**, 021301.